

An asymptotic model of particle deposition at an airway bifurcation

JENNIFER R. ZIERENBERG

Department of Biomedical Engineering, University of Michigan, Ann Arbor, MI 48109, USA

DAVID HALPERN*

Department of Mathematics, University of Alabama, Tuscaloosa, AL 35487, USA

*Corresponding author: dhalpern@as.ua.edu

MARCEL FILOCHE AND BERNARD SAPOVAL

Laboratoire de Physique de la Matière Condensée, Ecole Polytechnique, Palaiseau 91128, France

JAMES B. GROTBORG

Department of Biomedical Engineering, University of Michigan, Ann Arbor, MI 48109, USA

[Received on 28 July 2011; revised on 22 December 2011; accepted on 19 January 2012]

Particle transport and deposition associated with flow over a wedge is investigated as a model for particle transport and flow at the carina of an airway bifurcation during inspiration. Using matched asymptotics, a uniformly valid solution is obtained to represent the high Reynolds number flow over a wedge that considers the viscous boundary layer near the wedge and the outer inviscid region and is then used to solve the particle transport equations. Sometimes particle impaction on the wedge is prevented due to the boundary layer. We call this boundary layer shielding (BLS). This effect can be broken down into different types: rejection, trapping and deflection that are described by what happens to the particle's initial negative velocity normal to the wall either changing sign, reaching zero, or remaining negative in the boundary layer region. The deposition efficiency depends on the critical Stokes number but exhibits a weak dependence on Reynolds number. Deposition efficiency for S_c in the range $0 < S_c < 0.4$ yields the following relationship $De \approx (1.867S_c^{1.78} - 0.016) \sin(\beta\pi/2)$ at large Reynolds numbers, where $\beta\pi$ is the wedge angle. For a specific deposition efficiency, S_c decreases as $\beta\pi$ increases. The distribution of impacted particles was also computed and revealed that particles primarily impact within one airway diameter of the carina, consistent with computational fluid dynamics approaches. This work provides a new insight that the BLS inherent to the wedge component of the structure is the dominant reason for the particle distribution. This finding is important in linking aerosol deposition to the location of airway disease as well as target sites for therapeutic deposition.

Keywords: pulmonary airways; particle deposition; deposition efficiency; wedge flow; boundary layer shielding; surfactants; airway closure.

1. Introduction

Micro- and nano particle transport and deposition in the human respiratory system is of particular interest in determining potential health effects of inhaled particles. These can be either harmful or therapeutic to humans depending on aerosol material, deposition site and local concentration. Toxic particulate matter or carcinogens are linked to lung disease while pharmaceuticals, to be used in medical

therapy, are being developed as part of targeted drug aerosol delivery systems (Heyder, 2004). An example of medical therapy relates to the treatment of prematurely born infants who lack sufficient surfactant. Because of this they have stiff lungs from the elevated surface tension and unstable airways that close by forming liquid plugs. Surfactant reduces the surface tension of the lung's liquid lining that stabilizes airways from closure (Halpern & Grotberg, 1993). Surfactant delivery into the lung can be from instillation of a surfactant as a liquid bolus directly into the trachea or endotracheal tube (Avery & Merritt, 1991; Stevens & Sinkin, 2007; Griese, 1999; Jobe, 1993). The instilled bolus propagates distally into the airways as a result of fluid dynamic, surface tension and gravity forces (Halpern *et al.*, 1998; Anderson *et al.*, 2004). Another delivery method is by surfactant aerosol deposition (Dhand, 2004; Ellyett *et al.*, 1996; Mazela *et al.*, 2007; Lewis & McCaig, 1993).

Deposition of aerosol particles in the lung is a complex process that is dependent on particle properties, geometric airway characteristics and ventilatory conditions. The complexity of the lung renders it difficult to perform direct experimental or computational studies of airflow and particle deposition. Instead, the respiratory airways of the lung are frequently approximated as a series of repeatedly bifurcating tubes and simple components of the system are considered.

A recent review of both experimental work and 2D and 3D numerical simulations of airflow and micro- and nano particle deposition and transport in airways can be found in Kleinstreuer *et al.* (2008). The computational fluid dynamics (CFD) literature on pulmonary aerosol deposition shows that most of the particles land near the carina of the bifurcations within one airway diameter of it along the medial wall of the daughter airways (Balashazy & Hofmann, 1993; Balashazy *et al.*, 1999; Kim & Iglesias, 1989; Gatlin *et al.*, 1997; Isaacs *et al.*, 2006; De Vasconcelos *et al.*, 2011). Yet, these computations do not examine the details of the local flow in that region. That flow has both a stagnation point and a developing boundary layer whose thickness depends mostly on the bifurcation angle and the Reynolds number, the ratio of inertial to viscous forces. In the present paper, a mathematical approach is used to isolate the key features of the flow at a carina and then to investigate the physics of the deposition behaviour and its dependence on the velocity field structure as well as particle properties. A similar strategy has been employed by Broday (2004) who modelled the deposition of ultra fine particles by diffusion near the carina and by Phillips & Kaye (1999) who investigated inertial particle deposition on a surface near a stagnation point flow.

In order to isolate and simplify the complex carinal flow, we choose to model flow over a wedge with aerosol deposition whose leading-order solution is the well-known Falkner–Skan flow (Schlichting & Gersten, 2000), without resorting to full CFD numerical simulations (Broday (2004) has compared the streamwise velocity of the Falkner–Skan flow for a 30° wedge with the CFD results of Comer *et al.* (2001b) and shown qualitatively good agreement for inspiratory flow near the carina). This is our basic flow regime and we extend it asymptotically to form a smooth velocity field from the inviscid to viscous boundary layer (Saintlos & Bretteville, 2002). With our analytical solution approach to the velocity field, we can apply the drag contribution from the velocities to a force balance on an aerosol particle in a straightforward process. From this detailed analysis of flow and deposition to the carinal region, we will elucidate a better understanding of a phenomenon we refer to as ‘boundary layer shielding’ (BLS). Since most impaction occurs near the carina, it is important to understand what shielding influences are present.

In Section 2, a description of the model is given. The flow field is solved using the method of matched asymptotics and the particle motion is determined by solving numerically a system of second-order ordinary differential equations. Results of the current model are described in Section 3, and conclusions are given in Section 4.

2. Model description

One of the significant fluid dynamical events during inspiration is the splitting of the flow field at an airway bifurcation. The flow encounters the airway carina, whose branch angle is $\beta\pi$, and passes on either side to the next generation in the tree, as shown in Fig. 1.

The range for β for large airways in the human lung is $1/3 < \beta < 1/2$ (Horsfield & Cumming, 1967). Two important parameters that can be used to describe the character of this flow field are the Reynolds number, Re , the ratio of inertial to viscous forces and the Womersley number, α , the ratio of flow unsteady acceleration to viscous effects. These are defined as

$$Re = \frac{\rho UD}{\mu}, \quad \alpha = D \left(\frac{\omega \rho}{\mu} \right)^{1/2},$$

where U is the average air velocity, D is the airway diameter, ρ is the air density, μ is the air viscosity and ω is the breathing frequency. The Reynolds number can range from 500 to 6800 in the larger airways (generations 0 to 4; Ultman, 1985), exceeding the critical value of 2300 required for the transition to turbulent flow in a smooth circular pipe. We restrict our attention to laminar flow, but the Reynolds number is sufficiently large so that viscous effects are not dominant except in a thin boundary layer where the velocity changes rapidly to zero in order to satisfy the no-slip condition at the airway wall. Normally, at high frequencies and in large airways, the Womersley number $\alpha > 1$. This would suggest that unsteady effects need to be included and the unsteady acceleration terms in the momentum equations cannot be neglected. However, numerical simulations by Li *et al.* (2007) have demonstrated that even for moderately large $\alpha \approx 2.3$, airflow patterns obtained during the inhalation phase of the breathing cycle are quite similar to those from steady-state computations at the same mean Reynolds number suggesting that a steady or quasi-steady approximation is reasonable provided the frequency is not high.

In CFD models of particle deposition, the parent and daughter tubes are modelled as cylinders that are joined by a ‘transition zone’. In this region, which includes the bifurcation, the carina is usually

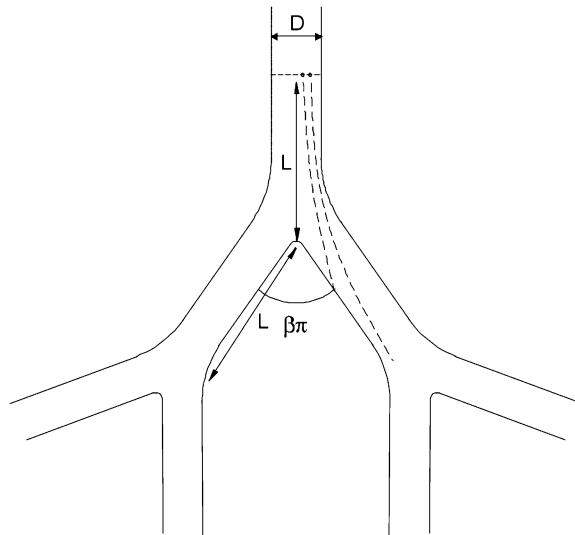


FIG. 1. Schematic of a bifurcation geometry, where D is the diameter of the parent tube, L is both the distance to the initial particle position line and the length of the daughter, $\beta\pi/2$ is the branching angle and U is a characteristic velocity in the parent tube.

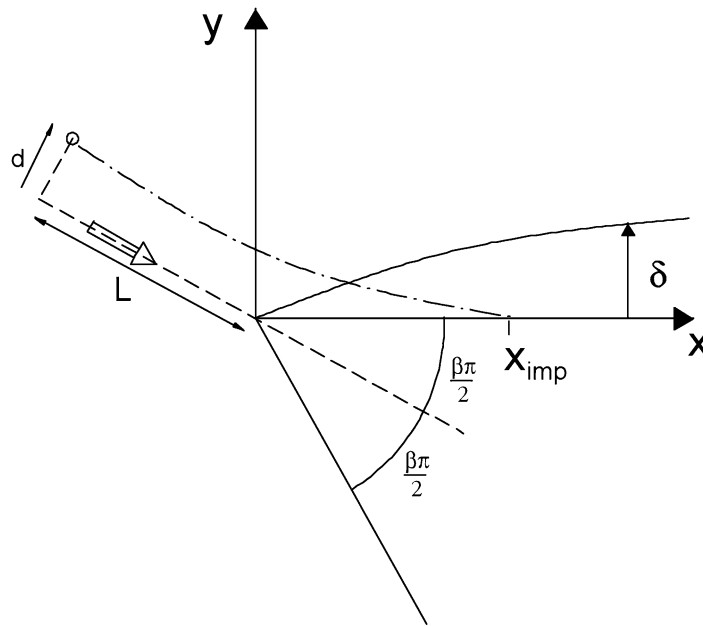


FIG. 2. Definition sketch for flow over a wedge subtending an angle $\beta\pi$ where δ is the boundary layer thickness. Here, d denotes the distance from the centreline from which a particle is released, and x_{imp} is the location of particle impact on the wedge.

modelled as a sharp wedge. For more details on the impact of airway bifurcation geometry on deposition, see, e.g. the papers by Balashazy & Hofmann (1993) and Balashazy *et al.* (1996). There are two flow regimes for high Reynolds number flow over a wedge. The region along the wedge surface has a viscous boundary layer that begins at the stagnation point and grows in the x -direction, parallel to one of the sides of the wedge as shown in Fig. 2. Flow in this region is governed by the relevant boundary layer equations. The region outside of the boundary layer is governed by inviscid fluid mechanics. It is possible to model these two regions separately and apply the resulting fluid drag on an aerosol particle depending on which region it is currently traversing. So a particle may start outside the boundary layer, the drag being defined on the basis of the inviscid fluid velocity relative to the particle velocity. Then it may enter the boundary layer and see a viscous flow regime with a new fluid velocity, and hence drag, environment. One could patch together a particle trajectory that crosses into the boundary layer by using the inviscid particle position at the boundary layer edge and its inviscid velocity as initial conditions to the particle path within the boundary layer. However, there is a jump in fluid velocity at the edge of the boundary layer with this approach. This jump is due to the boundary layer approximation such that the inviscid, x -velocity on the wall ($y = 0$) must be x^n , to satisfy the criteria for Falkner–Skan flow that simplifies the boundary layer analysis into one involving a similarity variable. For the boundary layer, the same criterion is applied for the boundary layer at its edge, $y = \delta(x)$. In the next section, a solution for the velocity field is derived which is uniformly valid in the boundary layer as well as the inviscid outer region.

2.1 Problem formulation

We derive the velocity field in the two regions described above: an inner region next to the wedge wall where viscous effects are important and an outer region that is dominated by inertial effects.

2.1.1 Velocity field

Outer region. The dimensionless Navier–Stokes and mass conservation equations are

$$\begin{aligned} u \frac{\partial u}{\partial x} + v \frac{\partial u}{\partial y} &= -\frac{\partial p}{\partial x} + \frac{1}{\text{Re}} \left(\frac{\partial^2 u}{\partial x^2} + \frac{\partial^2 u}{\partial y^2} \right), \\ u \frac{\partial v}{\partial x} + v \frac{\partial v}{\partial y} &= -\frac{\partial p}{\partial y} + \frac{1}{\text{Re}} \left(\frac{\partial^2 v}{\partial x^2} + \frac{\partial^2 v}{\partial y^2} \right), \\ \frac{\partial u}{\partial x} + \frac{\partial v}{\partial y} &= 0, \end{aligned} \tag{2.1}$$

where x and y are scaled on the characteristic length, taken to be the parent tube diameter, D , as in Fig. 1; u and v are scaled on the characteristic velocity in the parent tube, U and p is scaled on ρU^2 , where ρ is the fluid density. The Reynolds number is $\text{Re} = \rho U D / \mu$, where μ is the fluid viscosity and is assumed to be large. Let $\varepsilon = 1 / \sqrt{\text{Re}}$ and pose the expansions (Van Dyke, 1975; Saintlos & Bretteville, 2002)

$$\begin{aligned} u(x, y) &= \tilde{u}_0(x, y) + \varepsilon \tilde{u}_1(x, y) + O(\varepsilon^2), \\ v(x, y) &= \tilde{v}_0(x, y) + \varepsilon \tilde{v}_1(x, y) + O(\varepsilon^2), \\ p(x, y) &= \tilde{p}_0(x, y) + \varepsilon \tilde{p}_1(x, y) + O(\varepsilon^2). \end{aligned} \tag{2.2}$$

In addition, it is convenient to introduce a stream function $\tilde{\psi}$ such that $u = \frac{\partial \tilde{\psi}}{\partial y}$ and $v = -\frac{\partial \tilde{\psi}}{\partial x}$. Then the continuity equation is automatically satisfied. As with the other dependent variables, we express $\tilde{\psi}$ as a power series in ε

$$\tilde{\psi}(x, y) = \tilde{\psi}_0(x, y) + \varepsilon \tilde{\psi}_1(x, y) + O(\varepsilon^2). \tag{2.3}$$

Outer region, $O(1)$. The leading-order system is the inviscid Euler equations and the continuity equation or the Laplace equation for the stream function since the vorticity is 0 at this order. The forms are

$$\begin{aligned} \tilde{u}_0 \frac{\partial \tilde{u}_0}{\partial x} + \tilde{v}_0 \frac{\partial \tilde{u}_0}{\partial y} &= -\frac{\partial \tilde{p}_0}{\partial x}, \\ \tilde{u}_0 \frac{\partial \tilde{v}_0}{\partial x} + \tilde{v}_0 \frac{\partial \tilde{v}_0}{\partial y} &= -\frac{\partial \tilde{p}_0}{\partial y}, \\ \frac{\partial \tilde{u}_0}{\partial x} + \frac{\partial \tilde{v}_0}{\partial y} &= 0, \\ \nabla^2 \tilde{\psi}_0 &= \frac{\partial^2 \tilde{\psi}_0}{\partial x^2} + \frac{\partial^2 \tilde{\psi}_0}{\partial y^2} = \frac{1}{r} \frac{\partial}{\partial r} \left(r \frac{\partial \tilde{\psi}_0}{\partial r} \right) + \frac{1}{r^2} \frac{\partial^2 \tilde{\psi}_0}{\partial \theta^2} = 0, \end{aligned} \tag{2.4}$$

where $r = \sqrt{x^2 + y^2}$ and $\theta = \tan^{-1} \left(\frac{y}{x} \right)$. The solution to the velocities at this order must comply with the requirement for a similarity solution to the boundary layer flow, i.e. the Falkner–Skan flow (described below), that

$$\begin{aligned}\tilde{u}_0(x, y = 0) &= x^n, \\ \tilde{v}_0(x, y = 0) &= 0.\end{aligned}\tag{2.5}$$

The solution to the Laplace equation (2.4) that satisfies these wall conditions is

$$\tilde{\psi}_0 = \frac{1}{n+1} r^{n+1} \sin((n+1)\theta),\tag{2.6}$$

where $n = \frac{\beta}{2-\beta}$ or $\beta = 2n/(1+n)$. Therefore, the leading-order inviscid velocity components are

$$\begin{aligned}\tilde{u}_0(x, y) &= r^n \cos(n\theta), \\ \tilde{v}_0(x, y) &= -r^n \sin(n\theta).\end{aligned}\tag{2.7}$$

The pressure field is obtained from Bernoulli's equation:

$$\tilde{p}_0 = -\frac{1}{2}(\tilde{u}_0^2 + \tilde{v}_0^2) = -\frac{1}{2}r^{2n}.\tag{2.8}$$

As an example, $n = 1$ ($\beta = 1$) yields inviscid stagnation point flow. Under these circumstances, (2.7) simplifies to the familiar form $\tilde{u}_0 = x$, $\tilde{v}_0 = -y$. Also, when $n = 0$ ($\beta = 0$), the result is uniform and parallel flow over a flat plate such that $\tilde{u}_0 = 1$, $\tilde{v}_0 = 0$. The bifurcation angle range of $1/3 < \beta < 1/2$ corresponds to $1/5 < n < 1/3$.

For the matching procedure, we will need the expansions of (2.7) and (2.8) in the limit $y \rightarrow 0$, which are

$$\begin{aligned}\tilde{u}_0(x, y) &= x^n - \frac{n(n-1)}{2} x^{n-2} y^2 + O(y^4), \\ \tilde{v}_0(x, y) &= -n x^{n-1} y + \frac{n(n-1)(n-2)}{6} x^{n-3} y^3 + O(y^5), \\ \tilde{p}_0 &= -\frac{1}{2} x^{2n} - \frac{n}{2} x^{2n-2} y^2 + O(y^4).\end{aligned}\tag{2.9}$$

Inner region. We rescale the vertical coordinate by defining the inner variable as $Y = y/\varepsilon$ to retain the viscous effects in a boundary layer next to the wall. The dependent variables in the boundary layer are given by the expansions

$$\begin{aligned}u(x, Y) &= U_0(x, Y) + \varepsilon U_1(x, Y) + O(\varepsilon^2), \\ v(x, Y) &= \varepsilon[V_0(x, Y) + \varepsilon V_1(x, Y) + O(\varepsilon^2)], \\ p(x, Y) &= P_0(x, Y) + \varepsilon P_1(x, Y) + O(\varepsilon^2).\end{aligned}\tag{2.10}$$

Inner region, $O(1)$. The leading-order system is

$$\begin{aligned}U_0 \frac{\partial U_0}{\partial x} + V_0 \frac{\partial U_0}{\partial Y} &= -\frac{\partial P_0}{\partial x} + \frac{\partial^2 U_0}{\partial Y^2}, \\ 0 &= -\frac{\partial P_0}{\partial Y},\end{aligned}\tag{2.11}$$

$$\frac{\partial U_0}{\partial x} + \frac{\partial V_0}{\partial Y} = 0,$$

whose solution is the Falkner–Skan flow

$$\begin{aligned} U_0(x, Y) &= x^n f'(\eta), \\ V_0(x, Y) &= -\frac{1}{2}x^{(n-1)/2}[(n+1)f(\eta) + (n-1)\eta f'(\eta)], \\ P_0(x, Y) &= -\frac{1}{2}x^{2n}, \end{aligned} \tag{2.12}$$

where $f(\eta)$ satisfies

$$\begin{aligned} f'''(\eta) + \frac{n+1}{2}ff'' + n(1-f'^2) &= 0, \\ f(0) = 0, \quad f'(0) = 0, \quad \lim_{\eta \rightarrow \infty} f'(\eta) &= 1, \end{aligned} \tag{2.13}$$

and $\eta = x^{(n-1)/2}Y$ is the similarity variable. The limiting forms of $f(\eta)$ as $\eta \rightarrow 0, \infty$ are needed for matching, and they are

$$f(\eta) \underset{\eta \rightarrow 0}{=} \frac{\lambda_n}{2}\eta^2 - \frac{n}{6}\eta^3 + O(\eta^5), \quad f(\eta) \underset{\eta \rightarrow \infty}{=} \eta + \nu_n + \text{EST}, \tag{2.14}$$

where EST are exponentially small terms. The constants λ_n and ν_n can be determined, respectively, by numerically evaluating

$$\begin{aligned} \lambda_n &= \lim_{\eta \rightarrow 0} f''(\eta), \\ \nu_n &= \lim_{\eta \rightarrow \infty} (f(\eta) - \eta). \end{aligned} \tag{2.15}$$

Outer region, $O(\varepsilon)$. The $O(\varepsilon)$ equations in the outer region are

$$\begin{aligned} \tilde{u}_0 \frac{\partial \tilde{u}_1}{\partial x} + \tilde{u}_1 \frac{\partial \tilde{u}_0}{\partial x} + \tilde{v}_0 \frac{\partial \tilde{u}_1}{\partial y} + \tilde{v}_1 \frac{\partial \tilde{u}_0}{\partial y} &= -\frac{\partial \tilde{p}_1}{\partial x}, \\ \tilde{u}_0 \frac{\partial \tilde{v}_1}{\partial x} + \tilde{u}_1 \frac{\partial \tilde{v}_0}{\partial x} + \tilde{v}_0 \frac{\partial \tilde{v}_1}{\partial y} + \tilde{v}_1 \frac{\partial \tilde{v}_0}{\partial y} &= -\frac{\partial \tilde{p}_1}{\partial y}, \\ \frac{\partial \tilde{u}_1}{\partial x} + \frac{\partial \tilde{v}_1}{\partial y} &= 0, \\ \nabla^2 \tilde{\psi}_1 &= 0. \end{aligned} \tag{2.16}$$

The $O(\varepsilon)$ pressure correction is derived from Bernoulli's equation and is given by

$$\tilde{p}_1(x, y) = -(\tilde{u}_0(x, y)\tilde{u}_1(x, y) + \tilde{v}_0(x, y)\tilde{v}_1(x, y)). \tag{2.17}$$

Because of the matching requirements described below as $y \rightarrow 0$, $\tilde{\psi}_1$ takes the form

$$\tilde{\psi}_1 = Cr^{m+1} \cos((m+1)\theta), \tag{2.18}$$

where C and m are constants to be determined. Therefore, the $O(\varepsilon)$ velocity corrections obtained from (2.18) are

$$\begin{aligned}\tilde{u}_1 &= -C(m+1)r^m \sin(m\theta), \\ \tilde{v}_1 &= -C(m+1)r^m \cos(m\theta).\end{aligned}\tag{2.19}$$

Inner region, $O(\varepsilon)$. The $O(\varepsilon)$ inner problem is given by

$$\begin{aligned}U_0 \frac{\partial U_1}{\partial x} + U_1 \frac{\partial U_0}{\partial x} + V_0 \frac{\partial U_1}{\partial Y} + V_1 \frac{\partial U_0}{\partial Y} &= -\frac{\partial P_1}{\partial x} + \frac{\partial^2 U_1}{\partial Y^2}, \\ 0 &= -\frac{\partial P_1}{\partial Y}, \\ \frac{\partial U_1}{\partial x} + \frac{\partial V_1}{\partial Y} &= 0.\end{aligned}\tag{2.20}$$

In order to solve the inner problem at $O(\varepsilon)$, we need to provide boundary and matching conditions. For the matching between the inner and outer regions, we need the limit of the inner solution as $Y \rightarrow \infty$:

$$\begin{aligned}\lim_{Y \rightarrow \infty} u(x, Y) &= x^n + \varepsilon \lim_{Y \rightarrow \infty} U_1(x, Y) + O(\varepsilon^2), \\ \lim_{Y \rightarrow \infty} v(x, Y) &= -\varepsilon n x^{n-1} Y - \varepsilon \frac{(n+1)}{2} v_n x^{(n-1)/2} + O(\varepsilon^2),\end{aligned}\tag{2.21}$$

and the outer solution as $y \rightarrow 0$

$$\begin{aligned}\lim_{y \rightarrow 0} \tilde{u}(x, y) &= x^n + \varepsilon \lim_{y \rightarrow 0} \tilde{u}_1(x, y) + O(\varepsilon^2), \\ \lim_{y \rightarrow 0} \tilde{v}(x, y) &= -n x^{n-1} y + \varepsilon \lim_{y \rightarrow 0} \tilde{v}_1(x, y) + O(\varepsilon^2).\end{aligned}\tag{2.22}$$

Equating the limits for each velocity component leads to

$$\begin{aligned}\lim_{Y \rightarrow \infty} U_0(x, Y) &= \lim_{y \rightarrow 0} \tilde{u}_0(x, y) = x^n, \\ \lim_{Y \rightarrow \infty} U_1(x, Y) &= \lim_{y \rightarrow 0} \tilde{u}_1(x, y), \\ \lim_{y \rightarrow 0} \tilde{v}_1(x, y) &= -\frac{(n+1)v_n}{2} x^{(n-1)/2}.\end{aligned}\tag{2.23}$$

Now we are in a position to determine uniquely the $O(\varepsilon)$ outer problem and provide some of the additional boundary conditions required to solve the $O(\varepsilon)$ inner problem. From (2.19), we must have $\tilde{v}_1 \rightarrow -C(m+1)x^m$ as $y \rightarrow 0$. Thus, $C = \frac{1}{2}(n+1)v_n$, $m = \frac{1}{2}(n-1)$ on applying (2.23). So the $O(\varepsilon)$ outer velocities are

$$\begin{aligned}\tilde{u}_1(x, y) &= \frac{(n+1)}{2} v_n \sin\left(\frac{1-n}{2}\theta\right) r^{(n-1)/2}, \\ \tilde{v}_1(x, y) &= -\frac{(n+1)}{2} v_n \cos\left(\frac{1-n}{2}\theta\right) r^{(n-1)/2}.\end{aligned}\tag{2.24}$$

We note that $\tilde{u}_1 \rightarrow 0$ as $y \rightarrow 0$, which provides a boundary condition on the $O(\varepsilon)$ inner problem. The $O(\varepsilon)$ outer pressure $\tilde{p}_1(x, y) \rightarrow 0$ as $y \rightarrow 0$ since $\tilde{u}_1 \rightarrow 0$ and $\tilde{v}_0 \rightarrow 0$ as $y \rightarrow 0$. Therefore,

$$P_1(x, Y) = 0 \tag{2.25}$$

because $\tilde{p}_1(x, y)$ and $P_1(x, Y)$ must match at the edge of the boundary layer and P_1 is independent of Y according to (2.20). The remaining velocity equations in (2.20) yield a third-order system of linear homogeneous partial differential equations for (U_1, V_1) . Its boundary conditions (in Y) are also homogeneous since $U_1(x, 0) = 0$, that is and $\lim_{Y \rightarrow \infty} U_1(x, Y) = 0$, and $V_1(x, 0) = 0$. Hence, both $O(\varepsilon)$ inner velocity components are zero, that is

$$U_1(x, Y) = V_1(x, Y) = 0.$$

Finally, we construct a uniformly valid composite solution by adding the inner and outer solutions up to $O(\varepsilon)$ and subtracting the values obtained due to the matching (so that they are not added twice). For the velocity components, these are given by

$$\begin{aligned} u_{\text{comp}} &= U_0(x, y) + \tilde{u}_0(x, y) - \tilde{u}_0(x, 0) + \varepsilon \tilde{u}_1(x, y), \\ v_{\text{comp}} &= \tilde{v}_0(x, y) + \varepsilon [\tilde{v}_1(x, y) + V_0(x, Y) - \tilde{v}_1(x, 0) + nx^{n-1}Y]. \end{aligned} \tag{2.26}$$

We define the composite velocity vector as $\underline{u}_{\text{comp}} = (u_{\text{comp}}, v_{\text{comp}})$.

2.2 Particle motion

An important parameter that plays a role in characterizing particle deposition is the Stokes number. According to Heyder (2004), total deposition is defined to be the probability that a particle is deposited in one of the airways. The mode of deposition is dependent on particle size and weight and the flow conditions. For nano-sized particles that have diameters $< 0.1 \mu\text{m}$, the primary mechanism for deposition is diffusion, while small micron particles, with diameters ranging from $0.1 \mu\text{m}$ to $1 \mu\text{m}$, are deposited mostly by sedimentation in the distal airways. Inertial impaction becomes the dominant mechanism for larger and heavier particles with diameters $> 1 \mu\text{m}$, primarily in the upper airways. The Stokes number is defined as the ratio of particle inertia to particle drag:

$$S = \frac{mU}{C_d D} = \frac{\rho_p d_p^2 U}{18\mu D},$$

where m is the particle mass, ρ_p is its density, $C_d = 3\pi\mu d_p$ is the Stokes drag coefficient and d_p is the particle diameter. Most of the previous investigations have considered a range of Stokes numbers from 0.02 to 0.3 (see, e.g. Zhang *et al.*, 2002). This is a reasonable range for particles with $1 \leq d_p \leq 10 \mu\text{m}$ and $0.5 \leq \rho_p \leq 5 \text{ g/cm}^3$ that are transported in the larger airways, such as generation three where the Reynolds number is of the order 1000 and the flow is laminar.

Scaling time on D/U , the equations of motion for an aerosol particle, whose position is at $(x_p(t), y_p(t))$, are

$$\begin{aligned} S \frac{d^2 x_p}{dt^2} &= u_{\text{comp}}(x_p, y_p) - \frac{dx_p}{dt}, \\ S \frac{d^2 y_p}{dt^2} &= v_{\text{comp}}(x_p, y_p) - \frac{dy_p}{dt}, \end{aligned} \tag{2.27}$$

where linear particle drag has been assumed and S is the Stokes number that has been defined above. The influence of non-linear drag following the methodology outlined in [Comer *et al.* \(2001a\)](#), [Zhang & Kleinstreuer \(2002\)](#) and [Yalcin *et al.* \(2007\)](#), which includes a linear regime for small local particle Reynolds number, Re_p , and a non-linear regime for large particle Reynolds number was found to be negligible in which $Re_p = \rho |\underline{u}_{\text{comp}} - \underline{u}_p| d_p / \mu$, where $\underline{u}_{\text{comp}}$ is the composite air velocity (see (2.26)) and $\underline{u}_p = \left(\frac{dx_p}{dt}, \frac{dy_p}{dt} \right)$ is the particle velocity. This is due to the small particle Reynolds numbers present in the current study where the difference between the fluid velocity and particle velocity is small since particle motion for only one generation as represented by a wedge is considered and the initial particle velocity is assumed to equal the fluid velocity at the starting point upstream from the wedge.

Our interest is to follow a set of particles that start along a diameter of the parent airway. We choose a diameter that is at a distance $L = 3D$ from the wedge vertex at its nearest point as shown in Fig. 2. The particle starts at a distance, d , from the centreline, and d will have values $0 \leq d \leq D/2$, assuming symmetry of the flow. Then the initial position scaled on D is

$$\begin{aligned} x_p(0) &= -3 \cos\left(\frac{\beta\pi}{2}\right) + \gamma \sin\left(\frac{\beta\pi}{2}\right), \\ y_p(0) &= 3 \sin\left(\frac{\beta\pi}{2}\right) + \gamma \cos\left(\frac{\beta\pi}{2}\right), \end{aligned} \quad (2.28)$$

where $\gamma = d/D$ so that $0 \leq \gamma \leq 0.5$. We assume that the initial particle velocity is equal to the fluid velocity at that point,

$$\begin{aligned} \frac{dx_p}{dt}(0) &= u_{\text{comp}}(x_p(0), y_p(0)), \\ \frac{dy_p}{dt}(0) &= v_{\text{comp}}(x_p(0), y_p(0)). \end{aligned} \quad (2.29)$$

The initial normal component of velocity $\underline{u}_{\text{comp}} \cdot \underline{n}$, where \underline{n} is the unit normal vector to the wall, is plotted in Fig. 3 as a function of γ , the distance from the centreline, for two different values of β corresponding to wedge angles of 60° ($\beta = 1/3$) and 90° ($\beta = 1/2$). The velocity is observed to increase with distance from the centreline and with wedge angle.

2.3 Particle motion in inviscid flow

In order to evaluate the influence of the boundary layer on particle motion for flow over a wedge, the inviscid velocity component is considered instead of the composite velocity in the above particle motion equations. As previously shown in (2.7) for inviscid flow, the velocity components are

$$\begin{aligned} u_{\text{inviscid}} &= \tilde{u}_0(x, y) = r^n \cos(n\theta), \\ v_{\text{inviscid}} &= \tilde{v}_0(x, y) = -r^n \sin(n\theta). \end{aligned} \quad (2.30)$$

The special case of stagnation point flow, with $n = 1$, has been previously studied by [Taylor \(1940\)](#), who found that there is a critical Stokes number of $1/4$ below which impaction does not occur. This special limit is derived by solving a second-order linear differential equation that is obtained by substituting the inviscid velocity field (2.3) into (2.27). [Phillips & Kaye \(1999\)](#) extended Taylor's work by considering the effect of a viscous boundary layer on this critical Stokes number.

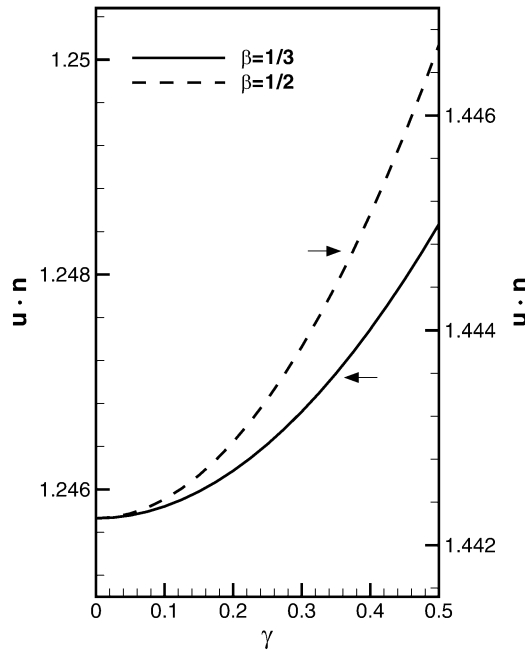


FIG. 3. The normal component of velocity $\underline{u}_{\text{comp}} \cdot \underline{n}$ along initial particle location given by (2.28), where $0 \leq \gamma \leq 0.5$. Arrows adjacent to each curve indicate the appropriate γ -axis. Here, \underline{n} is the unit normal vector to the wall.

2.4 Method of solution

The Falkner–Skan equation (2.13) was solved following the methodology developed by Asaithambi (2004). In this method, a coordinate transformation maps the semi-infinite domain into a finite domain. The transformed equation is then approximated using second-order finite differencing and the resulting non-linear system of equations is solved iteratively. In order to solve the particle motion equations (2.27), it is necessary to know the composite velocities (2.26) at any position. This requires one to interpolate the solution of the Falkner–Skan equation, which needs to only be solved once. The particle motion equations are then solved using a Runge–Kutta solver.

3. Results

3.1 The flow field

In Figs. 4–7, we show some velocity profiles computed using the method described above for representative wedge angles and Reynolds numbers and the differences between the inner region and outer region flow fields. The difference between Figs. 4 and 5 (and Figs. 6 and 7) lies with the value of x , the distance along the wedge measured from the vertex scaled by the tube diameter D . As is well known, the boundary layer thickens with increasing x due to the increased friction, and hence there is a larger discrepancy between the inviscid tangential component of velocity u_0 and the composite component u_{comp} as shown in Fig. 5(a) compared to that shown in Fig. 4(a). Figures also indicate a small discrepancy between the composite solution and the inviscid solution outside the boundary layer if only the leading-order inviscid solution is used.

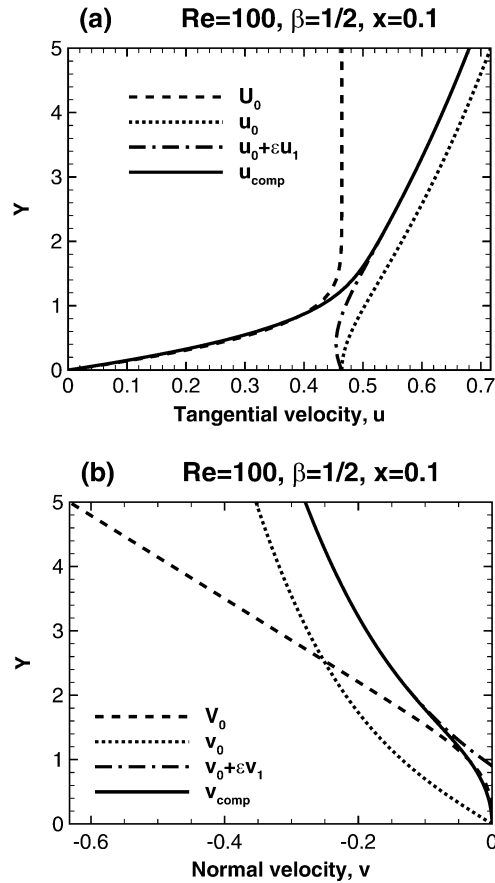


FIG. 4. (a) Tangential, u and (b) normal, v , components of velocity across the boundary layer and into the outer region at $x = 0.1$ for $\beta = 1/2$ and $Re = 100$. Here, (u_0, v_0) and (U_0, V_0) are the leading-order inviscid and boundary layer velocities, and (u_{comp}, v_{comp}) is the composite velocity.

However, this difference is significantly diminished if the two-term inviscid solution is used instead. Of significance for particle deposition on the wedge surface is the normal velocity component, v_{comp} . For some values of β , e.g. $\beta = 1/2$, v_{comp} is negative for all $Y = y/\epsilon$ as shown in Figs. 4(b) and 5(b), while for other values of β , such as $\beta = 1/3$, v_{comp} is positive near the wall (Figs. 6(b) and 7(b)). Therefore, for $\beta = 1/3$, particles may be pushed away from the wall.

In order to follow the motion of an aerosol particle, (2.27) is solved numerically subject to the initial conditions given by (2.28) and (2.29). As shown in Fig. 3, the initial normal velocity component is almost uniform.

The effect of the wedge angle on the particle trajectory near the wedge for $Re = 100$, $\log(S) = -0.62$ and $\gamma = 0.05$ is shown in Fig. 8. The outer edge of the boundary layer, i.e. the boundary layer thickness, is also shown. This is the distance from the wall to a point where the velocity is 99% of the free stream value.

Only one line is shown for the boundary layer, though in actuality the boundary layer thickness increases with decreasing wedge angle. However, for the range displayed in Fig. 8, the lines for all

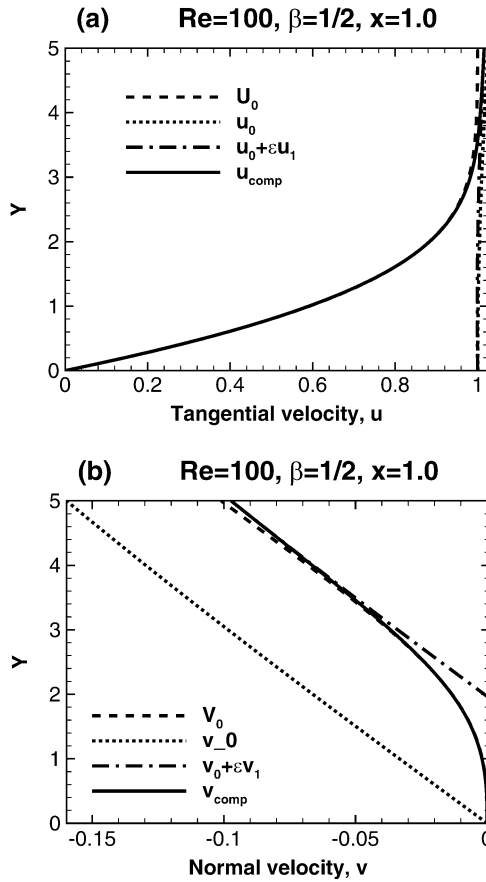


FIG. 5. (a) Tangential and (b) normal components of velocity at $x = 1$ for a wedge with $\beta = 1/2$ and for $Re = 100$.

wedge angles lie approximately on top of each other. In all instances, particle impaction is not observed, but instead the particle passes to the next generation. This is due to the influence of the boundary layer and a phenomenon that we describe as BLS is observed, whereas for a purely inviscid flow, particle impaction would result in all instances.

The BLS effect can be broken down into three different types: rejection, where the particle enters the boundary layer with a negative normal component of velocity ($v_p < 0$) and is kicked back (with $v_p > 0$) passing to the next generation; trapping, where the particle enters the boundary layer with $v_p < 0$ but later $v_p = 0$ so that the particle does not leave the boundary layer and passes to the next generation and deflection, where the particle approaches the boundary layer with $v_p < 0$ and continues to only have $v_p < 0$ and passes on to the next generation. All three instances are observed in Fig. 8 where rejection occurs for $\beta = 1/3$ and $5/12$, trapping for $\beta = 1/2$ and deflection for $\beta = 7/12$. The trapping ($\beta = 1/2$) case is shown again in Fig. 9. In addition, the trajectory followed by a particle using the two-term inviscid velocity field and the displacement thickness are displayed. The displacement thickness is defined as the distance by which streamlines that lie just outside the boundary layer are displaced and is given by the following formula:

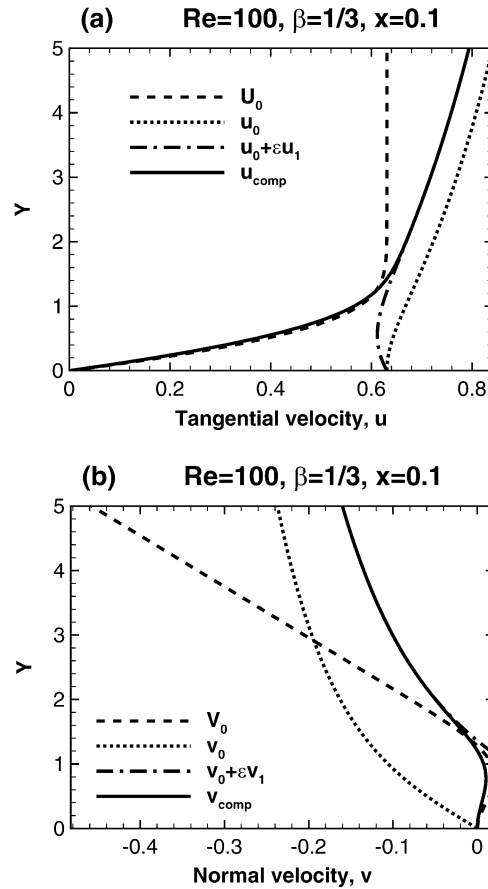


FIG. 6. Tangential and (b) normal components of velocity at $x = 0.1$ for a wedge angle with $\beta = 1/3$ and for $Re = 100$.

$$\delta = \int_0^{\infty} \left(1 - \frac{U_0}{\tilde{u}_0}\right) dy = -\epsilon v_n x^{(1-\beta)/(2-\beta)}. \quad (3.1)$$

Once the particle enters the boundary layer, the trajectories followed by a particle using the full composite solution and the two-term inviscid solution begin to deviate, with the two-term inviscid solution trajectory closely tracking the displacement thickness. Figure 10 shows the streamlines using the composite, the leading-order inviscid and the two-term inviscid solutions. Outside the boundary layer, the three cases agree as expected, but inside it, the two-term inviscid streamlines have a positive y component of velocity. Therefore, it can be inferred that the two-term inviscid velocity field component must be responsible for turning the y -velocity component from negative to positive in the rejection cases.

3.2 Particle deposition

The particle deposition efficiency represents the ratio of the number of particles deposited in an airway to the total number entering the airway. Particle deposition efficiencies are computed as follows, where

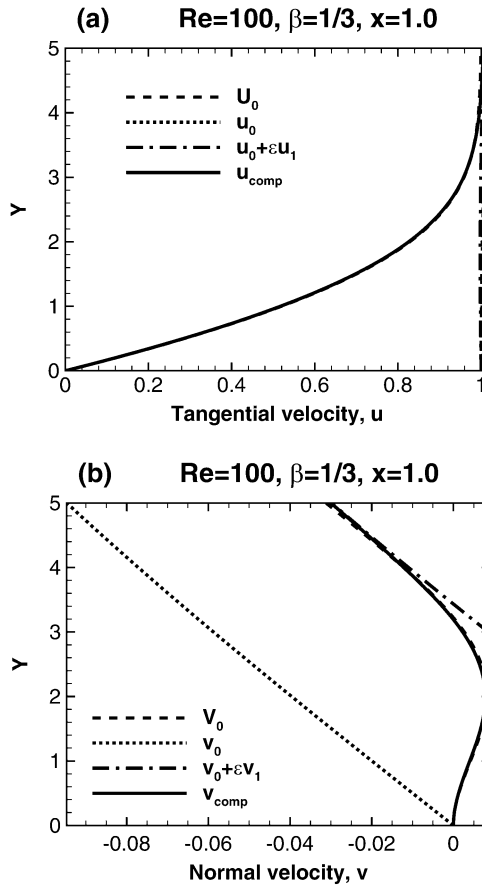


FIG. 7. (a) Tangential and (b) normal components of velocity at $x = 1$ for a wedge with $\beta = 1/3$ and for $Re = 100$.

a uniform particle distribution in the parent airway is assumed. Choosing a value of $\gamma = \gamma_0$, where $0 \leq \gamma_0 \leq 0.5$, sets the initial particle position. Then we select a value for the Reynolds number, Re , and search for the smallest value of the Stokes number S that causes the particle to impact the wall at $x_{imp} \leq 3$. In the lung application, the airway length is typically three times the diameter, so a particle that does not impact within this distance goes on to the next generation and its wedge flow. This value of S is the critical value, $S_c(\gamma_0)$ and all particles with $\gamma < \gamma_0$ when $S = S_c(\gamma_0)$ will also land on the wall. That makes the ratio $\gamma_0/0.5$ equal to the deposition efficiency, De , for this value of S_c . Deposition efficiencies are discussed later.

Mapping of the different BLS effects in $\beta - S$ parameter space for $\gamma = 0.005, 0.05$ and 0.25 is shown in Fig. 11 for (a) $Re = 100$, (b) $Re = 500$ and (c) $Re = 1000$. The impact lines separate particles that impact (above line) from particles that pass to the next generation (below line) for purely inviscid flow and flow when the boundary layer is considered.

BLS occurs in between these two impact lines and is characterized into rejection, trapping and deflection regions. The dot-dash line ($\cdot - \cdot -$) separates the rejection and trapping regions, while the dot-dot-dashed line ($\cdot \cdot -$) separates the trapping and deflection regions. Rejection is observed for small

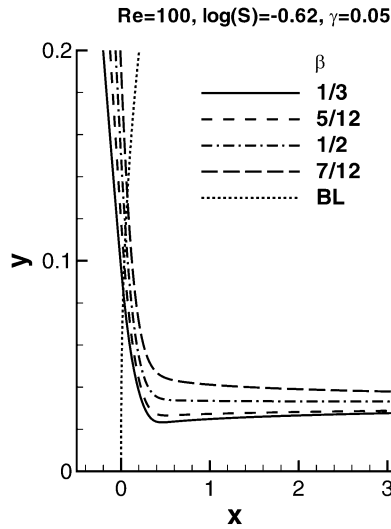


FIG. 8. Effect of wedge angle on particle trajectory for $Re = 100$, $\log(S) = -0.62$, $\gamma = 0.05$, where the different types of BLS can be observed: rejection ($\beta = 1/3$ and $5/12$), trapping ($\beta = 1/2$) and deflection ($\beta = 7/12$). The dotted line represents the outer edge of the boundary layer, i.e. the boundary layer thickness.

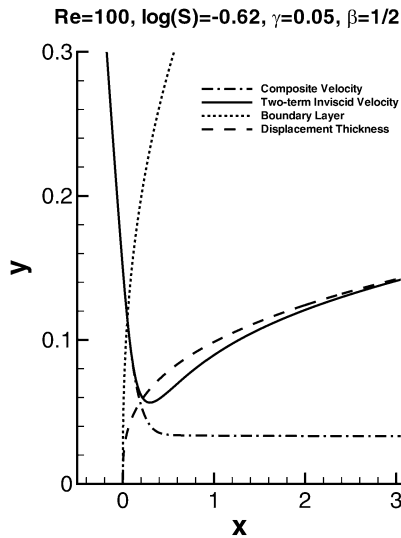


FIG. 9. Effect of velocity on particle trajectory for $Re = 100$, $\log(S) = -0.62$, $\gamma = 0.05$, $\beta = 1/2$, where the trajectories of a particle subject to the composite velocity versus the two-term inviscid velocity are compared.

β with γ near the centre of the parent airway ($\gamma = 0.005$ and 0.05) for S slightly smaller than S_c and is detected for nearly all cases of Re investigated with the exception of $Re = 100$ where only trapping is observed for $\gamma = 0.005$. For $\gamma = 0.05$, the area of the BLS characterized by rejection and deflection decreases with increasing Re , while the trapping region increases. For $\gamma = 0.25$, the area of the BLS characterized by trapping decreases, while the deflection region increases with Re . Only deflection is observed for $\gamma = 0.25$ and $Re = 1000$. As Re increases, the inviscid solution is approached and the BLS

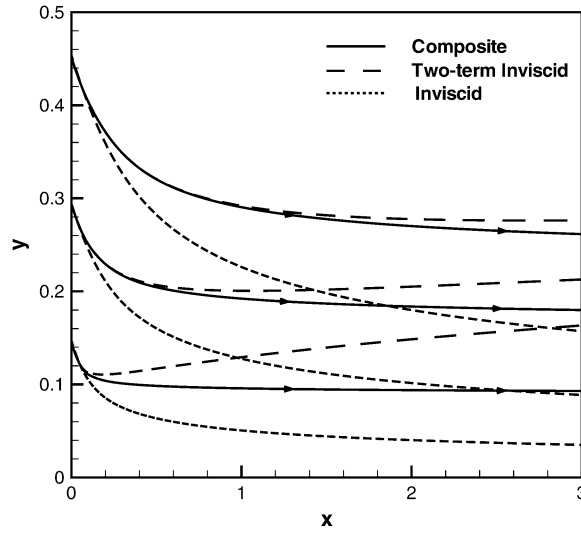


FIG. 10. Streamlines for composite velocity, two-term inviscid velocity and inviscid velocity for $Re = 100$.

region decreases. While not shown, the separation of the BLS effects for $Re = 1500$ is similar to that obtained for $Re = 1000$ (Fig. 11(c)).

Figure 12 shows the effect of the Stokes number on the particle trajectory near the wedge for $\beta = 1/3$, $Re = 100$ and $\gamma = 0.05$ as well as the location of the outer edge of the boundary layer and displacement thickness. There is a critical S above which the particle hits the wall. This happens when $\log(S) = -0.54$. For a slightly lighter particle, with $\log(S) = -0.55$, the particle almost hits the wall, but the positive normal component of fluid velocity near the wall causes the particle to gradually move away from the wall. This velocity effect is even more significant at smaller values of S . The boundary layer offers a shielding effect that results in rejection. Particle trajectories and the outer edge of the boundary layer and displacement thickness for a larger wedge angle, $\beta = 1/2$, are shown in Fig. 13. For this angle, the normal component of velocity is always negative, but a sufficiently light particle does not hit the wall in the range $x \leq 3$. Instead particles are trapped in the boundary layer where $v_p = 0$.

Deposition efficiencies for $\beta = 1/3$ and $\beta = 1/2$ are shown in Figs. 14 and 15, respectively, for $0.025 < S_c < 0.4$. The deposition efficiency appears to be an exponential function of the critical Stokes number with a very small dependence on Reynolds number. For a given Re , the deposition efficiency curve for $\beta = 1/3$ is shifted to the right of that for $\beta = 1/2$. The dependence on β is discussed later in this section. We have also compared our current results for deposition efficiency with those obtained from a computational model (Lee *et al.*, 1996) and from experiments (Kim & Fisher, 1999). Lee *et al.* (1996) provide computational data for 2D ducts with a branching angle of 45° ($\beta = 1/2$). The ducts had a square cross-section, and the ratio of parent to daughter duct cross-sectional area was 1.25^2 . Kim & Fisher (1999) used a more realistic 3D model to represent the third, fourth and fifth airways generations. In their model, the branching angle was 30° ($\beta = 1/3$) and the ratio of parent tube to daughter tube diameter was approximately 1.2.

Care must be taken with the definition of the velocity scale in the Stokes number when making comparisons. In our model, the initial starting position of the particles is three parent tube diameters from the carina, and the velocity is almost uniform. However, in the other models (Lee *et al.*, 1996; Kim & Fisher, 1999), the particles are inserted at the inlet to the parent tube where the fluid velocity

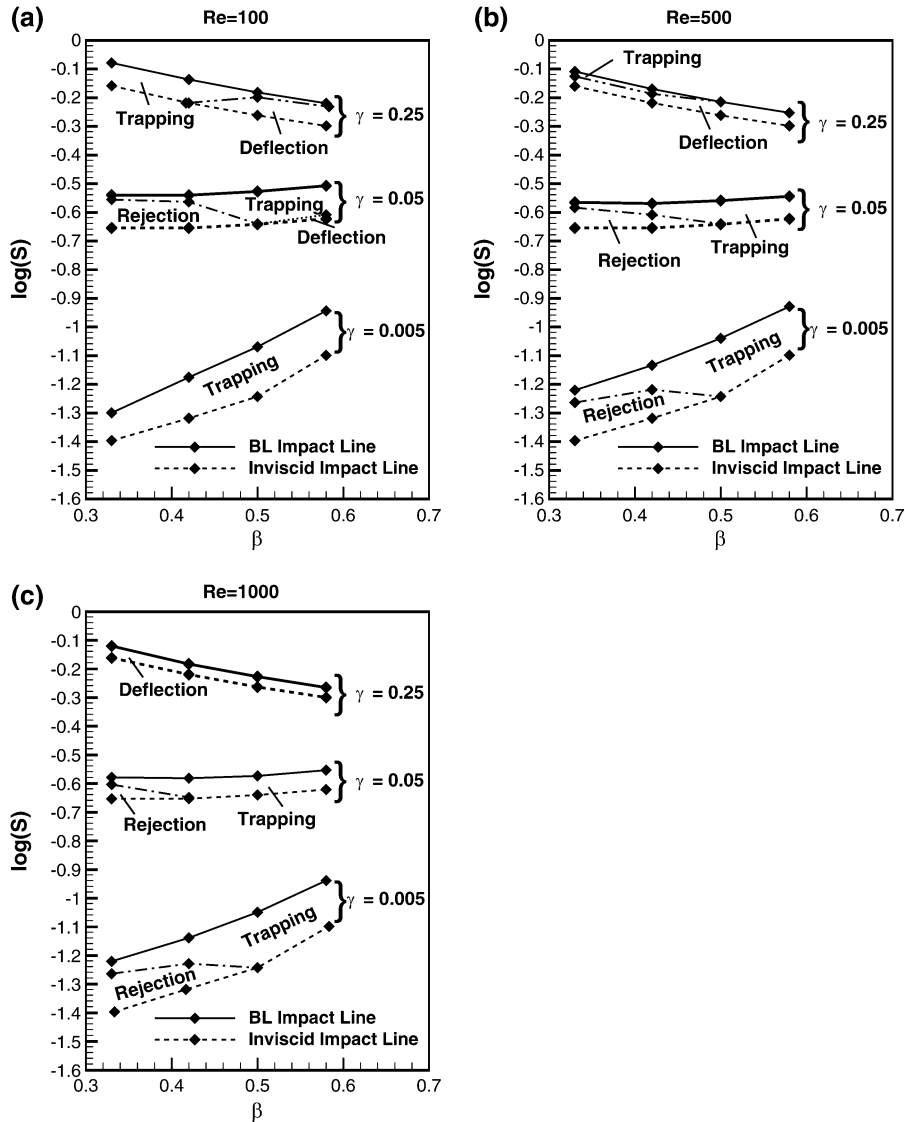


FIG. 11. Mapping of BLS in β - S parameter space with $\gamma = 0.05, 0.25$ and 0.5 into rejection, trapping and deflection regions for (a) $Re = 100$, (b) $Re = 500$ and (c) $Re = 1000$. The impact lines separate particles that impact (above line) from particles that pass to the next generation (below line) for purely inviscid flow and flow when the boundary layer is considered. The dot-dash line (·-·-) separates the rejection and trapping regions while the dotted line (· · ·) separates the trapping and deflection regions.

is prescribed to be parabolic. The mean velocity near the carina is smaller than that at the inlet since the cross-sectional area is larger near the carina. Let A_1 and A_2 be the total cross-sectional areas of the parent and daughter tubes. Then $A_1 = \pi D_1^2/4$ and $A_2 = 2\pi D_2^2/4$, where D_1 and D_2 are the diameters of the parent and daughter tubes, respectively. By mass conservation, $\bar{u}_1 A_1 = \bar{u}_2 A_2$, where \bar{u}_1 and \bar{u}_2 are the mean velocities in the parent and daughter tubes. Therefore, the ratio \bar{u}_1/\bar{u}_2 is given by

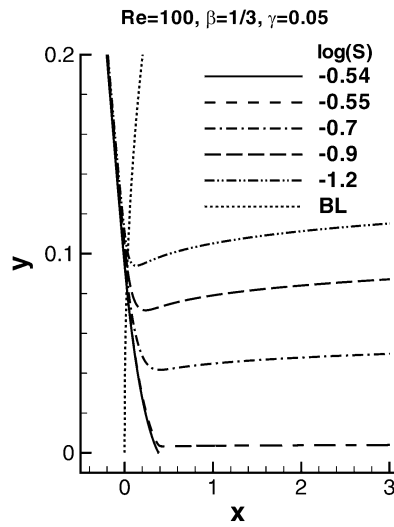


FIG. 12. Effect of Stokes number on particle trajectory for $Re = 100, \beta = 1/3$ and $\gamma = 0.05$.

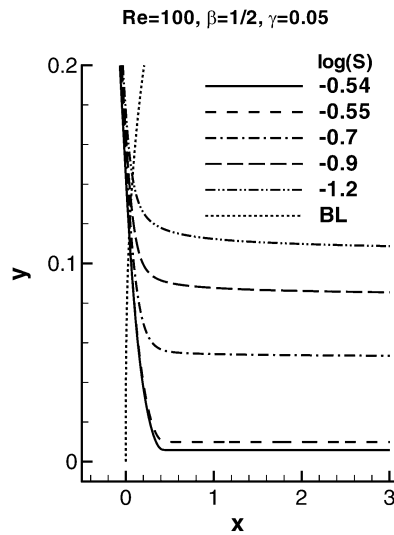


FIG. 13. Effect of Stokes number on particle trajectory for $Re = 100, \beta = 1/2$ and $\gamma = 0.05$.

$$\frac{\bar{u}_1}{\bar{u}_2} = \frac{A_2}{A_1} = 2 \left(\frac{D_2}{D_1} \right)^2.$$

For the 2D computational model of Lee *et al.* (1996), the ratio of inlet mean velocity to mean velocity near the carina is approximately 1.28, while for the 3D model of Kim & Fisher (1999), this ratio is 1.4. In Fig. 14, a function relating deposition efficiency to Stokes number used by Kim & Fisher (1999) to fit their experimental data has also been plotted. This function is of the form

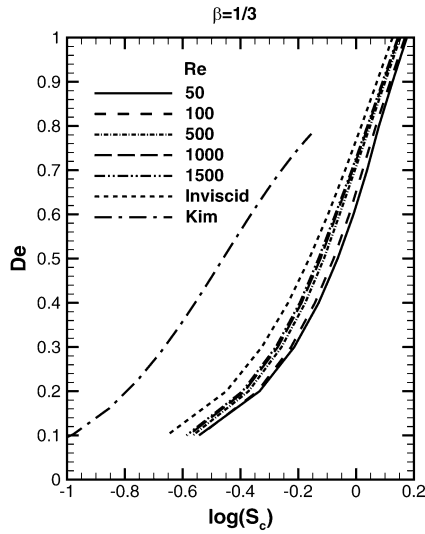


FIG. 14. Dependence of deposition efficiency on the critical Stokes number and the Reynolds number for $\beta = 1/3$.

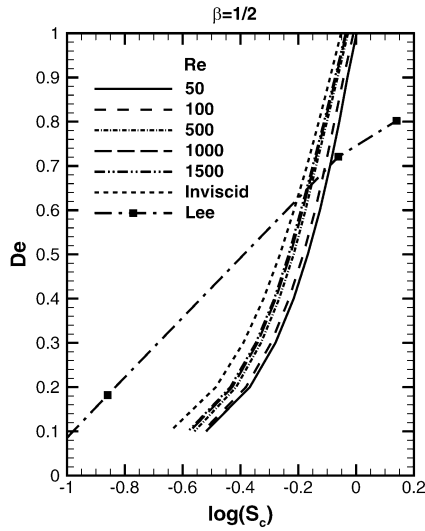


FIG. 15. Dependence of deposition efficiency on the critical Stokes number for $\beta = 1/2$.

$$De = 1 - \frac{1}{aSt^b + 1},$$

where $a = 12.68$ and $b = 1.819$. In Fig. 15, for the wedge angle with $\beta = 1/2$, we have included several data points joined by straight lines (as in Fig. 4 of Lee *et al.*, 1996). The original data from Lee *et al.* (1996) and Kim & Fisher (1999) have been altered to account for the different definitions of the Stokes number as described above. Agreement is reasonably good between our model and the 2D model (Lee *et al.*, 1996). The discrepancy between our model and the curve fit based on the experimental

data of Kim & Fisher (1999) can be attributed to several factors besides the difference in the flow rates. It has been previously established that the type of inlet velocity profile can have a significant impact on the deposition efficiency no matter what computational model is used (Zhang *et al.*, 1997). More significantly, in the experiments and in the 3D computational models, the velocity field is 3D and secondary flows exist in the vicinity of the carina. Also, in our model, the velocity field does not satisfy the no-slip condition at the outer wall and a simpler model for particle motion is used.

Comer *et al.* (2000) fit their deposition efficiency data with a function De that depends on the critical Stokes number and the Reynolds number in the following way:

$$De(S_c, Re) = A(1 + cS_c^b)e^{mRe}, \tag{3.2}$$

where $0 < De < 1$. For $mRe \ll 1$, we can expand the exponent and find that

$$De(S_c, Re) \approx A(1 + cS_c^b)(1 + mRe). \tag{3.3}$$

We apply the non-linear least squares method to the data shown in Figs. 14 and 15 and determine the coefficients (A, b, c, m) in (3.3). For $\beta = 1/3$, we find that

$$(A, b, c, m) = (-0.0036, 1.47, -174.33, 0.00017),$$

while for $\beta = 1/2$, we find that

$$(A, b, c, m) = (-0.026, 1.64, -40.26, 0.00014).$$

The data show that $0.007 \leq mRe \leq 0.26$, so the assumption $mRe \ll 1$ is consistent. Equation (3.3) can be rearranged in the following way:

$$\log \left| \frac{De}{A} \right| = \log |1 + cS_c^b| + \log |1 + mRe| \approx \log |1 + cS_c^b| + mRe. \tag{3.4}$$

To check how well (3.4) fits the data, we show in Fig. 16 scatter plots of De versus $\log |1 + cS_c^b| + mRe$ for two wedge angles, with $\beta = 1/3$ and $\beta = 1/2$, respectively.

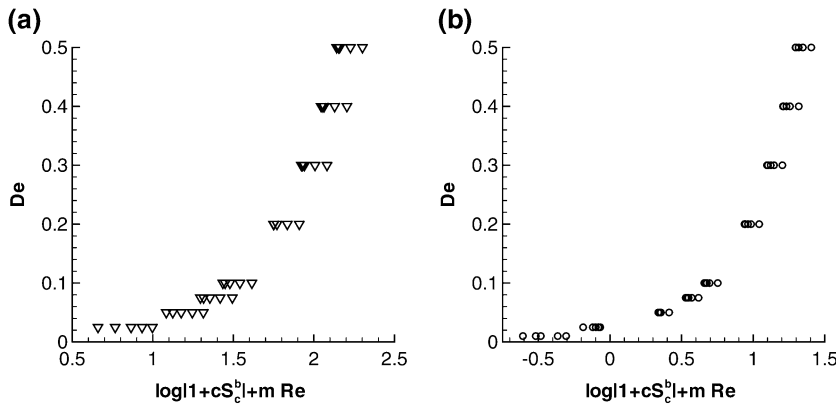


FIG. 16. Scatter plot showing how well deposition efficiency data fit (3.4) for (a) $\beta = 1/3$ and (b) $\beta = 1/2$. The parameters b, c and m are given in the text.

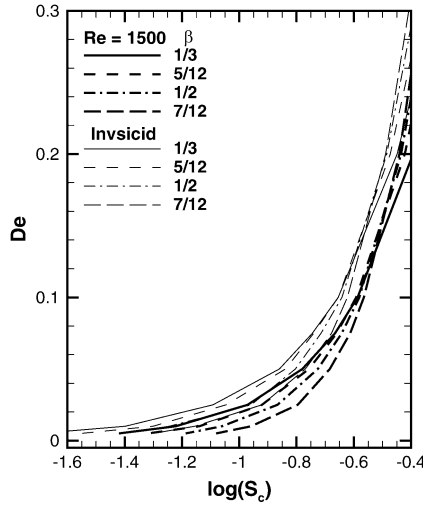


FIG. 17. Deposition efficiency versus the log of the critical Stokes number for different wedge angles for $Re = 1500$ and inviscid flow.

The dependence of the deposition efficiency on the wedge angle $\beta\pi$ for $Re = 1500$ is shown in Fig. 17. The corresponding deposition efficiency for inviscid flow is also shown for comparison. For the smallest critical Stokes numbers investigated ($\log S_c \approx -0.65$), the influence of wedge angle on deposition efficiency is almost negligible. While for larger critical Stokes numbers, the deposition efficiency curve shifts to the left with increasing wedge angle. For particle motion in stagnation point flow ($\beta = 1$), the deposition efficiency is approximately a linear function of the critical Stokes number.

In addition to the fit used above for fixed Re , see (3.2), we include a dependence on β (Cai & Yu, 1988):

$$De(S_c, \beta) = A(1 + cS_c^b) \sin(\beta\pi/2). \quad (3.5)$$

The above equation can be rearranged in the following way:

$$\log |De/A| = \log |1 + cS_c^b| + \log |\sin \beta\pi/2|.$$

We use non-linear least squares to find the coefficients A , b and c . For the data shown in Fig. 17 with $Re = 1500$

$$A = -0.016, \quad b = 1.78, \quad c = -116.7.$$

As shown in Fig. 18, this functional form for De fits our data reasonably well. Agreement between deposition efficiency data for other Reynolds numbers and (3.5) is also good (with coefficients A , b and c depending on the choice of Re).

The relative distribution of particles deposited on the airway wall due to impaction for $Re = 1500$ and $\log S = -0.473$ is shown for a 60° wedge in Fig. 19(a) and for a 90° wedge with $\log(S) = -0.434$ in Fig. 19(b). The x_{imp} intervals used are constant with the exception of the last interval that is smaller due to the maximum x_{imp} location. The corresponding deposition efficiencies are $De = 0.15$ and $De = 0.2$, respectively. As shown, the particles primarily impact near the airway carina, i.e. wedge

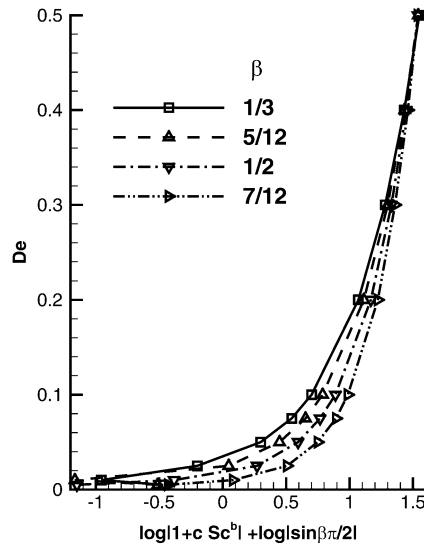


FIG. 18. Collapse of deposition efficiency data with respect to the critical Stokes number and the wedge angle for $Re = 1500$.

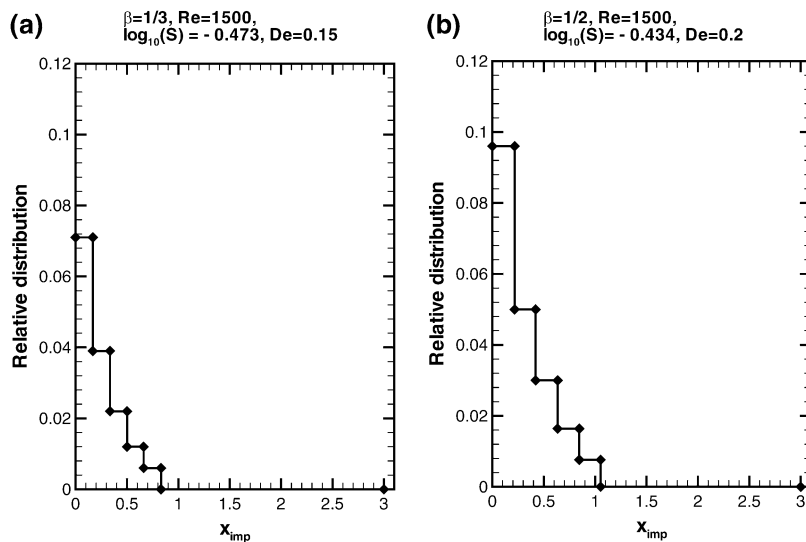


FIG. 19. Relative distribution of location of particle deposition for (a) $\beta = 1/3$ and (b) $\beta = 1/2$ for $Re = 1500$.

tip, with a greater number for the 90° wedge angle. For these parameters, there is a critical x_{imp} beyond which impaction does not occur and instead the remaining airborne particles travel to the next airway generation. This critical distance occurs at or very near $x_{imp} \sim 1$, i.e. the particles impact within one airway diameter of the carina as has been noted in complex CFD calculations (Balashazy & Hofmann, 1993; Balashazy *et al.*, 1999; Kim & Iglesias, 1989; Gatlin *et al.*, 1997; Isaacs *et al.*, 2006). Our model retains this very important feature and suggests that what is observed in full CFD approaches for

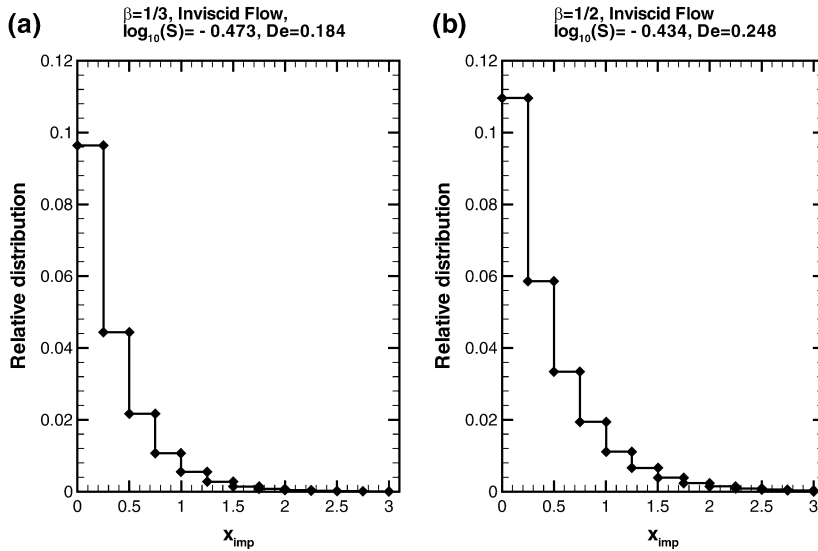


FIG. 20. Relative distribution of location of particle deposition for inviscid flow (a) $\beta = 1/3$ and (b) $\beta = 1/2$.

deposition near the carina can be explained from a detailed study such as ours with an analytical solution and BLS.

The relative impacted particle distribution for inviscid flow is shown for a 60° wedge in Fig. 20(a) and for a 90° wedge in Fig. 20(b) with deposition efficiencies of $De = 0.184$ and $De = 0.248$, respectively. The Stokes numbers in Fig. 20 are the same as those shown in Fig. 19. As before, the particles primarily impact near the carina, but in contrast to the viscous case, there is also particle impaction along the entire airway length ($0 < x_{\text{imp}} \leq 3$). So BLS as discussed above protects, the distal two-thirds of the airway length from exposure to particles.

4. Conclusion

Particle transport and deposition associated with flow over a wedge has been investigated as a model for particle transport and flow in the vicinity of an airway bifurcation carina. We identified three forms of BLS that prevent a particle from impacting at a generation, so they pass on to the next. Rejection requires a strong enough positive normal fluid velocity in the boundary layer to turn the particle around. This mechanism is more prevalent, then, at smaller wedge angles that have this feature. Deflection, on the other hand, is more a function of the boundary layer thickness when there is a weaker positive normal fluid velocity. In that case, the particle is still advancing towards the wall but cannot traverse the full thickness of the boundary layer in time to impact. Note that thicker boundary layers accompany larger wedge angles. It should be noted that deflection or trapping at a small wedge angle can occur for sufficiently heavy particles at high Reynolds numbers ($Re > 100$), while lighter particles for the same wedge angle will be rejected. Trapping is an intermediate situation that has contributions from both mechanisms.

We would like to stress that our focus here was to describe the BLS effect that occurs once particles are fairly close to the carinal wall and not to present a detailed model of the airflow through the lung's airways. In actuality, flow through the airways is 3D and far more complicated with secondary flow existing that cannot be captured in the present 2D study. Other limitations of the present model include

the investigation of a single airway bifurcation that does not consider the outer wall or subsequent airways and the assumption of a uniform non-transient inlet velocity. Yet, our results are similar to the CFD studies that include tube (3D or 2D) bifurcation geometries (parent and daughter tubes) in terms of deposition distribution. So our work provides a new insight that the BLS inherent to the wedge component of the structure is the dominant reason for the deposition distribution that is focused within one airway diameter of the carina. Our approach lends itself to further investigations. It is worthwhile pointing out that in our recent work (De Vasconcelos *et al.*, 2011), we have shown using a 3D CFD model that the particle capture process in a particular generation can be essentially independent of the capture in other airways despite the fact that airway particle deposition is a complex process.

Funding

This work was supported by Ecole Polytechnique, ANR Project (ANR-05-P032), Ecole Normale Supérieure de Cachan during J. B. Grotberg's sabbatical in 2006 and by the National Institutes of Health (NIH HL85156).

REFERENCES

- ANDERSON, J. C., MOLTHEN, R. C., DAWSON, C. A., HAWORTH, S. T., BULL, J. L., GLUCKSBERG, M. R. & GROTBORG, J. B. (2004) Effect of ventilation rate on instilled surfactant distribution in the pulmonary airways of rats. *J. Appl. Physiol.*, **97**, 45–56.
- ASAITHAMBI, A. (2004) A second-order finite-difference method for the Falkner-Skan equation. *Appl. Math. Comput.*, **156**, 779–786.
- AVERY, M. E. & MERRITT, T. A. (1991) Surfactant replacement therapy. *New Engl. J. Med.*, **324**, 910–911.
- BALASHAZY, I., HEISTRACHER, T. & HOFMANN, W. (1996) Air flow and particle deposition patterns in bronchial airway bifurcations: the effect of different CFD models and bifurcation geometries. *J. Aerosol Med. Deposition Clearance Effects Lung*, **9**, 287–301.
- BALASHAZY, I. & HOFMANN, W. (1993) Particle deposition in airway bifurcations. 1. Inspiratory flow. *J. Aerosol Sci.*, **24**, 745–772.
- BALASHAZY, I., HOFMANN, W. & HEISTRACHER, T. (1999) Computation of local enhancement factors for the quantification of particle deposition patterns in airway bifurcations. *J. Aerosol Sci.*, **30**, 185–203.
- BRODAY, D. M. (2004) Deposition of ultra fine particles at carinal ridges of the upper bronchial airways. *Aerosol Sci. Technol.*, **38**, 991–1000.
- CAI, F. S. & YU, C. P. (1988) Inertial and interceptional deposition of spherical-particles and fibers in a bifurcating airway. *J. Aerosol Sci.*, **19**, 679–688.
- COMER, J. K., KLEINSTREUER, C., HYUN, S. & KIM, C. S. (2000) Aerosol transport and deposition in sequentially bifurcating airways. *J. Biomech. Eng. Trans ASME*, **122**, 152–158.
- COMER, J. K., KLEINSTREUER, C. & KIM, C. S. (2001a) Flow structures and particle deposition patterns in double-bifurcation airway models. Part 2. Aerosol transport and deposition. *J. Fluid Mech.*, **435**, 55–80.
- COMER, J. K., KLEINSTREUER, C. & ZHANG, Z. (2001b) Flow structures and particle deposition patterns in double-bifurcation airway models. Part 1. Air flow fields. *J. Fluid Mech.*, **435**, 25–54.
- DE VASCONCELOS, T. F., SAPOVAL, B., ANDRADE, J. S. JR., GROTBORG, J. B., HU, Y. & FILOCHE, M. (2011) Particle capture into the lung made simple? *J. Appl. Physiol.*, **110**, 1664–1673.
- DHAND, R. (2004) New frontiers in aerosol delivery during mechanical ventilation. *Respir. Care*, **49**, 666–677.
- ELLYETT, K. M., BROADBENT, R. S., FAWCETT, E. R. & CAMPBELL, A. J. (1996) Surfactant aerosol treatment of respiratory distress syndrome in the spontaneously breathing premature rabbit. *Pediatr. Res.*, **39**, 953–957.
- GATLIN, B., CUICCHI, C., HAMMERSLEY, J., OLSON, D. E., REDDY, R. & BURNSIDE, G. (1997) Particle paths and wall deposition patterns in laminar flow through a bifurcation. *ASME FEDSM97*, Vancouver, BC, Canada. vol. 3434, 1–7.

- GRIESE, M. (1999) Pulmonary surfactant in health and human lung diseases: state of the art. *Eur. Respir. J.*, **13**, 1455–1476.
- HALPERN, D. & GROTBORG, J. B. (1993) Surfactant effects on fluid-elastic instabilities of liquid-lined flexible tubes: a model of airway closure. *J. Biomech. Eng. Trans. ASME*, **115**, 271–277.
- HALPERN, D., JENSEN, O. E. & GROTBORG, J. B. (1998) A theoretical study of surfactant and liquid delivery into the lung. *J. Appl. Physiol.*, **85**, 333–352.
- HEYDER, J. (2004) Deposition of inhaled particles in the human respiratory tract and consequences for regional targeting in respiratory drug delivery. *Proc. Am. Thorac. Soc.*, **1**, 315–320.
- HORSFIELD, K. & CUMMING, G. (1967) Angles of branching and diameters of branches in human bronchial tree. *Bull. Math. Biophys.*, **29**, 245.
- ISAACS, K. K., SCHLESINGER, R. B. & MARTONEN, T. B. (2006) Three-dimensional computational fluid dynamics simulations of particle deposition in the tracheobronchial tree. *J. Aerosol Med. Deposition Clearance Effects Lung*, **19**, 344–352.
- JOBE, A. H. (1993) Pulmonary surfactant therapy. *New Engl. J. Med.*, **328**, 861–868.
- KIM, C. S. & Iglesias, A. J. (1989) Deposition of inhaled particles in bifurcating airway models: I. Inspiratory deposition. *J. Aerosol Med.*, **2**, 1–14.
- KIM, C. S. & FISHER, D. M. (1999) Deposition characteristics of aerosol particles in sequentially bifurcating airway models. *Aerosol Sci. Technol.*, **31**, 198–220.
- KLEINSTREUER, C., ZHANG, Z. & LI, Z. (2008) Modeling airflow and particle transport/deposition in pulmonary airways. *Respir. Physiol. Neurobiol.*, **163**, 128–138.
- LEE, J. W., GOO, J. H. & CHUNG, M. K. (1996) Characteristics of inertial deposition in a double bifurcation. *J. Aerosol Sci.*, **27**, 119–138.
- LEWIS, J. F. & MCCAIG, L. (1993) Aerosolized versus instilled exogenous surfactant in a nonuniform pattern of lung injury. *Am. Rev. Respir. Dis.*, **148**, 1187–1193.
- LI, Z., KLEINSTREUER, C. & ZHANG, Z. (2007) Simulation of airflow fields and microparticle deposition in realistic human lung airway models. Part II: Particle transport and deposition. *Eur. J. Mech. B-Fluid*, **26**, 650–668.
- MAZELA, J., MERRITT, T. A. & FINER, N. N. (2007) Aerosolized surfactants. *Curr. Opin. Pediatr.*, **19**, 155–162.
- PHILLIPS, C. G. & KAYE, S. R. (1999) The influence of the viscous boundary layer on the critical Stokes number for particle impaction near a stagnation point. *J. Aerosol Sci.*, **30**, 709–718.
- SAINTLOS, S. & BRETTEVILLE, J. (2002) A uniformly valid approximation for a Falkner-Skan flow. *Comptes Rendus Mecanique*, **330**, 673–682.
- SCHLICHTING, H. & GERSTEN, K. (2000) *Boundary-Layer Theory*. Berlin, Germany: Springer.
- STEVENS, T. P. & SINKIN, R. A. (2007) Surfactant replacement therapy. *Chest*, **131**, 1577–1582.
- TAYLOR, G. I. (1940) Notes on possible equipment and technique for experiments on icing on aircraft. *Collected Works of G.I. Taylor.*, **3**, 236–243.
- ULTMAN, J. S. (1985) Gas transport in the conducting airways. *Gas Mixing and Distribution in the Lung* (L. A. Engel & M. Paiva eds). New York: Dekker.
- VAN DYKE, M. (1975) *Perturbation Methods in Fluid Mechanics*. Stanford, CA: Parabolic Press.
- YALCIN, H. C., PERRY, S. F. & GHADIALI, S. N. (2007) Influence of airway diameter and cell confluence on epithelial cell injury in an in-vitro model of airway reopening. *J. Appl. Physiol.*, **103**, 1796–1807.
- ZHANG, L., ASGHARIAN, B. & ANJILVEL, S. (1997) Inertial deposition of particles in the human upper airway bifurcations. *Aerosol Sci. Technol.*, **26**, 97–110.
- ZHANG, Z. & KLEINSTREUER, C. (2002) Transient airflow structures and particle transport in a sequentially branching lung airway model. *Phys. Fluids*, **14**, 862–880.
- ZHANG, Z., KLEINSTREUER, C. & KIM, C. S. (2002) Gas-solid two-phase flow in a triple bifurcation lung airway model. *Int. J. Multiphase Flow*, **28**, 1021–1046.